AGU PUBLICATIONS

JGR

Journal of Geophysical Research: Space Physics

RESEARCH ARTICLE

10.1002/2014JA020307

Key Points:
- The ENA flux from Martian magnetic anomaly region is higher
- Deviation of ion velocity and enhanced neutral density near MAs may explain
- Magnetic anomaly strongly modifies sheath plasmas and/or neutral atmosphere

Correspondence to:
X.-D. Wang,
wang@irf.se

Citation:
Wang, X.-D., S. Barabash, Y. Futaana, A. Grigoriev, and P. Wurz (2014), Influence of Martian crustal magnetic anomalies on the emission of energetic neutral hydrogen atoms, *J. Geophys. Res. Space Physics*, *119*, 8600–8609, doi:10.1002/2014JA020307.

Received 17 JUN 2014
Accepted 16 SEP 2014
Accepted article online 18 SEP 2014
Published online 14 OCT 2014

Influence of Martian crustal magnetic anomalies on the emission of energetic neutral hydrogen atoms

X.-D. Wang[1], S. Barabash[1], Y. Futaana[1], A. Grigoriev[2], and P. Wurz[3]

[1]Swedish Institute of Space Physics, Kiruna, Sweden, [2]Space Research Institute, Moscow, Russia, [3]Physikalisches Institut, University of Bern, Bern, Switzerland

Abstract We analyze the data on hydrogen energetic neutral atoms (ENAs) emissions from the dayside of Mars, recorded by a Neutral Particle Detector of the Analyzer of Space Plasmas and Energetic Atoms aboard Mars Express from 14 March to 9 July 2004. We first identify and analyze events of the ENA flux enhancement coinciding with the presence of the crustal magnetic anomalies on the dayside of Mars. We then backtrace the ENA emissions to the lower altitudes (source region) and build up an average map of the flux intensities in the geographic coordinates with all the available data. The map shows a peak-to-valley ENA flux enhancement of 40%–90% close to the crustal magnetic anomaly regions. These results suggest the influence of the magnetic anomalies on the ENA emission from the dayside of Mars. The enhancement may result from the deviation of the highly directional plasma flow above anomalies toward the detectors such that more charge exchange ENAs would be recorded. Alternatively, higher exospheric densities above the anomalies would also result in an increase of the charge exchange ENA flux.

1. Introduction

Energetic neutral atoms (ENAs) are mainly generated via charge exchange reactions between ions and neutral particles in a background neutral gas [cf. *Futaana et al.*, 2011]. ENAs preserve the velocities of their parent ions and thus can be used to diagnose the plasma remotely because the ENA production rate is proportional to the product of the ion flux and the neutral particle density. At Mars, ENA measurements so far have been used to study the basic generation mechanisms of ENAs [*Gunell et al.*, 2006a; *Futaana et al.*, 2006a; *Galli et al.*, 2008], the ion dynamics in the subsolar region [*Futaana et al.*, 2006a; *Grigoriev et al.*, 2006], and the response of the Martian-induced magnetosphere to extreme space weather condition [*Futaana et al.*, 2006b] and to constrain exospheric gas profiles [*Galli et al.*, 2008]. In this study, we investigate the effects of the Martian magnetic anomalies [*Acuña et al.*, 1998] on the ENA production.

The crustal magnetic anomalies discovered by Mars Global Surveyor [*Acuña et al.*, 1998] affect the local solar wind and ionospheric plasmas and may even impact the neutral atmosphere. The magnetic anomalies locally change the plasma flow of the shocked solar wind, which has been observed on numerous occasions. For example, the magnetic anomalies form the minimagnetosphere and cusp-like fields respectively in the closed and open field line regions [*Mitchell et al.*, 2001; *Ness et al.*, 2000; *Krymskii et al.*, 2002]. They also elevate the induced magnetosphere boundary (IMB) [*Crider et al.*, 2002; *Brain et al.*, 2005; *Dubinin et al.*, 2006]. Moreover, the magnetic anomalies allow the magnetosheath electrons to precipitate in the cusp-like regions [*Ness et al.*, 2000; *Krymskii et al.*, 2002; *Soobiah et al.*, 2006] and restrict the vertical diffusion of ionospheric electrons in the closed field line regions [*Soobiah et al.*, 2006; *Brain et al.*, 2007]. The parameters and/or chemical states of the neutral atmosphere over the magnetic anomalies could be influenced by the varied plasma flux. There are very few observations of this effect, only *Krymskii et al.* [2003, 2004] reported increase of the upper atmosphere temperature above the anomalies. All these modifications on plasma and/or neutral characteristics may affect the ENA emission near magnetic anomalies. The goal of this paper is to investigate how the magnetic anomalies affect the ENA emissions.

This paper is organized as follows: section 2 introduces the instrument and the selection of data. Section 3 shows two typical cases when a large-scale anomaly was within and outside the ENA detector field of view (FOV). In section 4 we present a map of the ENA emissions from the dayside hemisphere of Mars and their correlation with the crustal magnetic field intensity. In section 5 we first discuss the observed correlation

between the ENA flux enhancement and the magnetic anomalies and propose two mechanisms producing the observed results. Section 6 summarizes the study.

2. Instrumentation and Data Selection

We use the data from Neutral Particle Detectors (NPDs), a component of the Analyzer of Space Plasma and Energetic Atoms (ASPERA-3) onboard Mars Express (MEX). NPD is composed of two identical sensors, referred to as NPD1 and NPD2. Each sensor is a time-of-flight (TOF) ENA energy spectrometer, which measures the count rate of incident ENAs as a function of their energy. The energy of an ENA is determined by measuring the TOF, which is the time spent to fly over a known distance. In the data, hydrogen ENAs can be distinguished by their much shorter TOF than heavier species. The TOF range of the instrument is 50–1900 ns, corresponding to 100 eV–10 keV energy range for hydrogen ENAs. The instrument can resolve the direction of an incident ENA as well. The intrinsic field of view (FOV) is $9° \times 90°$, divided into three sectors (Dir0, Dir1, and Dir2) with an angular resolution $\sim 5° \times 40°$ (full width at half maximum). The two sensors are mounted such that their FOV planes are $\pm 15°$ away from the nadir direction and perpendicular to the spacecraft velocity when the spacecraft is in the nadir pointing mode. NPD operates as a 6 pixel ENA telescope facing Mars with an instantaneous FOV of $9° \times 180°$. For more details, see *Barabash et al.* [2006].

We use the data obtained in the so-called "binning" mode, the main operation mode when the most part of the data was obtained before the NPD operation was ceased in August 2004 [*Grigoriev*, 2007]. The actual coverage of valid data is from 14 March to 9 July 2004. In this mode, an ENA TOF (energy) spectrum, which is the ENA count rate as a function of the TOF (energy), is measured in 16 TOF (energy) steps for each sector at a rate of one spectrum per second.

We choose the TOF (energy) range from 100 to 309 ns (0.3–3 keV) to calculate the flux of hydrogen ENAs as in *Grigoriev et al.* [2006], because almost all hydrogen ENAs are within this range [e.g., *Mura et al.*, 2008; *Futaana et al.*, 2011]. No oxygen ENAs are expected within this range, because it would require unrealistically high energy of the parent oxygen ions (>5 keV) in the region of the high neutral density [*Barabash et al.*, 2002; *Futaana et al.*, 2011]. In addition, no oxygen ENAs have been clearly identified from Mars [*Galli et al.*, 2006].

3. Case Studies

3.1. Nominal Case: No Anomaly

Figure 1 shows a typical observation with little influence from the crustal magnetic field on the ENA emission, which is called "the nominal case" hereafter. This orbit was on 10 June 2014, and the observation period was from 22:23 UT to 22:52 UT. The spacecraft moved northward from the equator with increasing altitude (Figure 1b). The local time of the spacecraft during this observation was about 08–10 A.M., and the observed area on the dayside surface of Mars was at a solar zenith angle (SZA) less than 45° (Figure 1a). During the period, the FOV of NPD1 "scanned" the dayside surface of Mars from ~20°S to ~20°N latitude. This geometry was typical for the operation period from late May to early July in 2004. In this orbit, the Dir1 sector of NPD1 sensor observed the longitude region 30–60°W, where there are no major magnetic anomalies. Moreover, almost the whole dayside hemisphere is free of strong crustal magnetic field (Figure 1b). This is an ideal case to learn the baseline response of the instrument without any potential influence of the crustal magnetic field. The space environment proxies, such as the upstream dynamic pressure (solar wind pressure (SWP)) [*Crider et al.*, 2003], the shifted $F_{10.7}$ flux (F107), and the solar energetic particle (SEP) level [*Futaana et al.*, 2008] are listed for further references. We assume they do not vary drastically during the period of the observation.

The dayside magnetosheath and magnetosphere are a source of charge exchange and backscattered ENAs [*Futaana et al.*, 2006a; *Gunell et al.*, 2006a; *Futaana et al.*, 2006c]. Figure 2a shows a TOF time spectrum of the ENAs observed by NPD1 Dir1 during the nominal case. The TOF spectrum is equivalent to the energy spectrum. We average 60 original spectra obtained within 1 min for better statistics and remove the UV background by subtracting the count rate in the last TOF channel (longest TOF) [*Futaana et al.*, 2006a] in the average spectrum. Then we integrate the differential flux intensity over 0.3–3 keV energy range in the average energy spectrum to get the directional flux in the unit of $cm^{-2}\ s^{-1}\ sr^{-1}$. The time series of the directional flux is shown in Figure 2b. The directional flux kept $1–2 \times 10^5\ cm^{-2}\ s^{-1}\ sr^{-1}$ before 22:35 UT and gradually decreased afterward. The constant flux indicates that the FOV of NPD1 Dir1 was fully covered by the

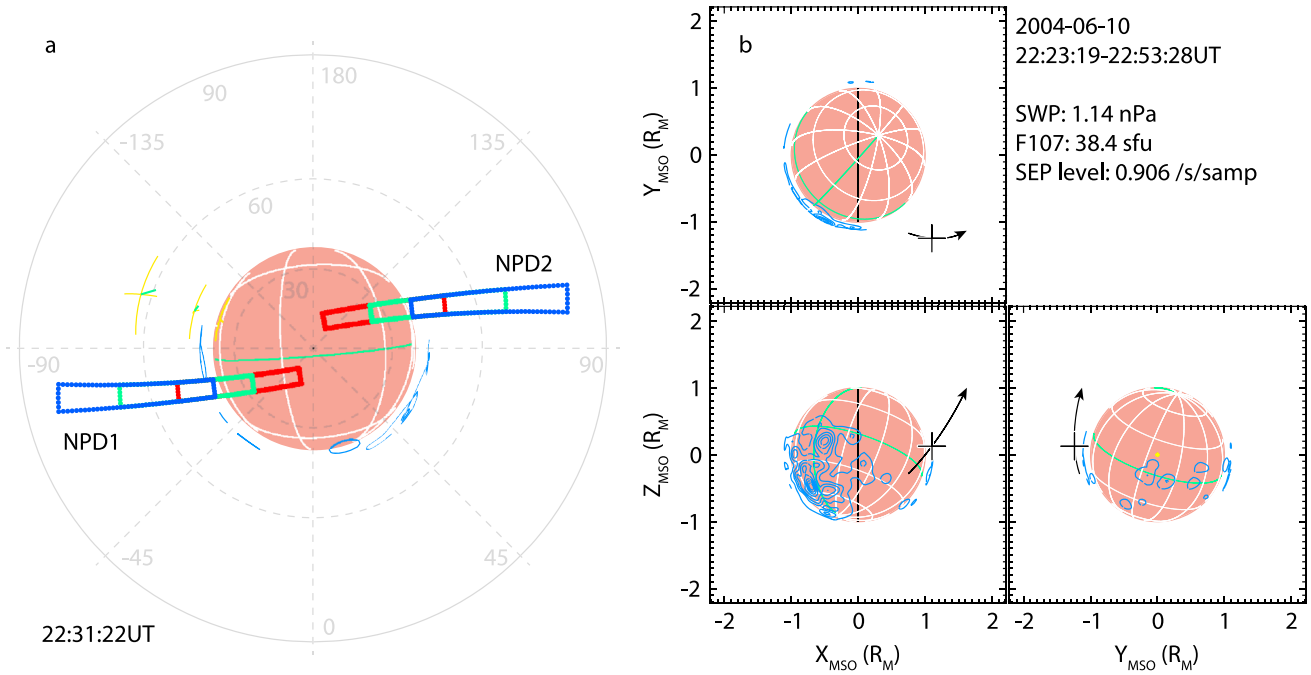

Figure 1. Observation geometry of the nominal case with little influence of the crustal magnetic field. (a) The observation geometry at 22:31:22 UT, 10 June 2004, shown in the instrument frame. The frame grid shows the elevation (cocentered circles) and azimuth (dashed lines crossing at the center) angles. Red, green, and blue quadrilaterals show the FOV of Dir0, Dir1, and Dir2 sectors for both sensors, respectively. The circle filled with dark red overlapped by white/green grids represents Mars with the grid in the geographic frame, and the green curve is the equator. The dark blue contour shows the distribution of the crustal magnetic field intensity at 400 km altitude. The yellow crosses show the subsolar points on the bow shock (farther left) and the induced magnetic boundary (IMB, closer to Mars). The short green line pointing out from a subsolar point mark shows the direction of the convective electric field. (b) The trajectory of the spacecraft (black curve with arrowhead) during the observation period in this orbit. Cross shows the position of the spacecraft at 22:31:22 UT. The black line at $X_{MSO} = 0$ represents the terminator. Space environment proxies: solar wind pressure (SWP) [*Crider et al.*, 2003], $F_{10.7}$ flux shifted from the Earth to Mars (F107), and solar energetic particle (SEP) level [*Futaana et al.*, 2008].

source region of ENAs; therefore, the measured differential flux intensity was kept the same as the spacecraft ascended. After 22:35 UT, the FOV gradually covered larger area with lower ENA production rate; therefore, the measured flux decreased. This flux decay is purely geometrical and was consistent for all orbits in the operation period. In this study, we focus on the constant flux in the early part of the observation.

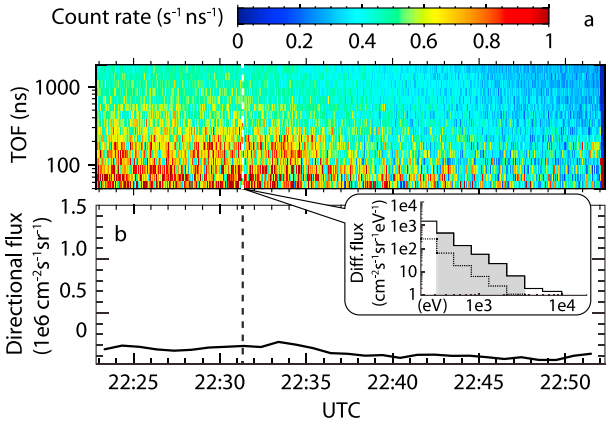

Figure 2. (a) Energy-time (E-t) spectrum of the raw ENA counts from NPD1 Dir1 during the observation period shown in Figure 1. (b) The directional flux calculated from the energy spectrum using the method described in section 2. Embedded: energy spectrum (solid line) of ENAs at the moment shown in Figure 1a (dashed lines in Figures 2a and 2b). The shaded bins are the energy range taken into account (0.3 keV–3 keV) in this study. The dotted line is the 1 count level.

3.2. Anomaly Case

Figure 3 shows an observation on the same day but from an earlier orbit than the nominal case. Since the two cases were only 20 h apart, the trajectory of the spacecraft with respect to the Sun-Mars line, hence the spacecraft local time, and the observation geometry kept almost unchanged. The space environment proxies were also very similar, especially the solar wind pressure that has been discovered to be the main influencing factor of ENA flux intensity [*Wang et al.*, 2013]. Although the convective electric field rotated by ~40°, the spacecraft was in the same hemisphere with respect to the electric field in both cases. Considering the variable nature of the space plasma environment, the influencing

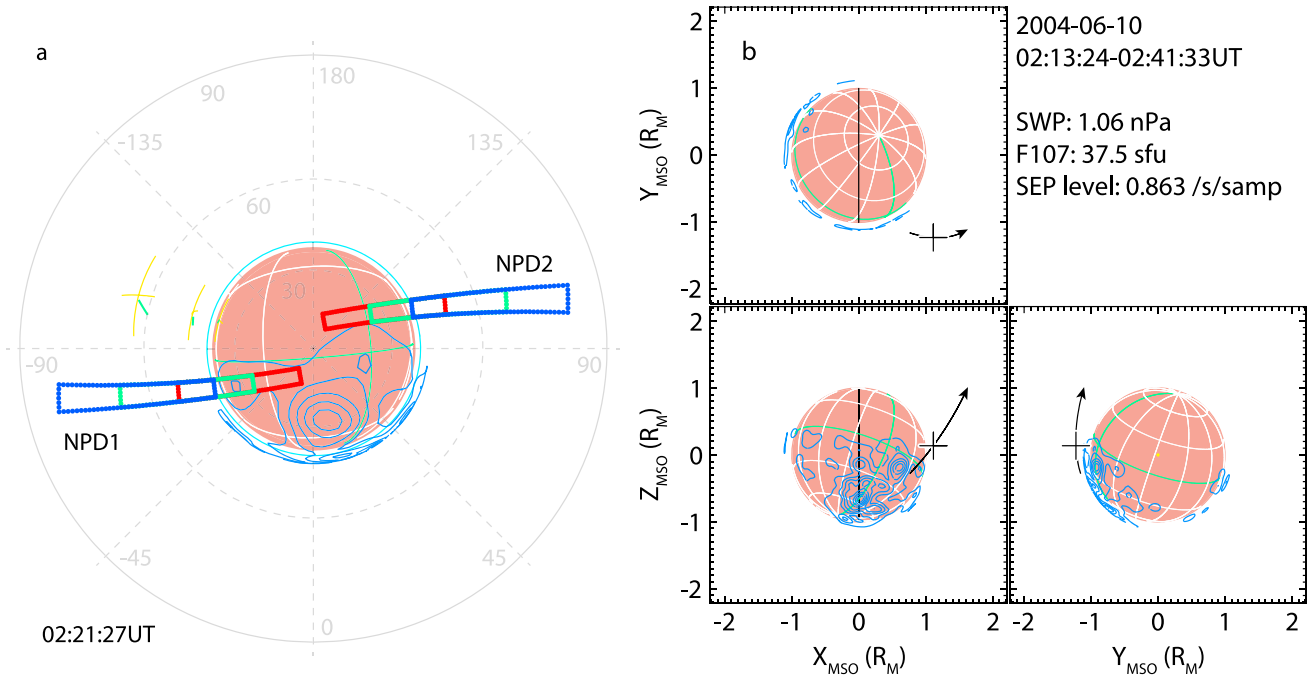

Figure 3. Observation geometry of the anomaly case with the influence of crustal magnetic field. The observation was from 02:13:24 to 02:41:33 UT on the same day as the nominal case. The structure of the figure is identical to that of Figure 1.

factors of these two cases were well constrained and similar. The critical difference between this case and the nominal case was the presence of the main magnetic anomalies in the NPD FOV. At the beginning of the observation, the spacecraft was above the strongest magnetic anomaly in the southern hemisphere. As the spacecraft later moved northward, the FOV of NPD1 scanned over the northern boundary of the anomaly region. One must note that the actual morphology of the magnetic fields are much more complicated and extended than the contours shown in Figure 3 [e.g., *Brain et al.*, 2003]. We call this case "the anomaly case" hereafter.

Figure 4 shows the time series of the TOF spectrum observed again by NPD1 Dir1, and the directional flux calculated by the same method. Both the differential flux intensity and the directional flux are much higher than those in the nominal case. The directional flux increased by a factor of ~4. As mentioned above, the observation geometry and the upstream conditions were maintained as well as possible during both observations, except for the different position of the magnetic anomalies with respect to the instrument. Despite of the variable nature of the ENA production process, we assume that the enhancement of ENA emissions is due to the presence of the crustal magnetic anomalies in the dayside hemisphere of Mars. We will verify this hypothesis drawn from the case study by the statistical results using the whole data set.

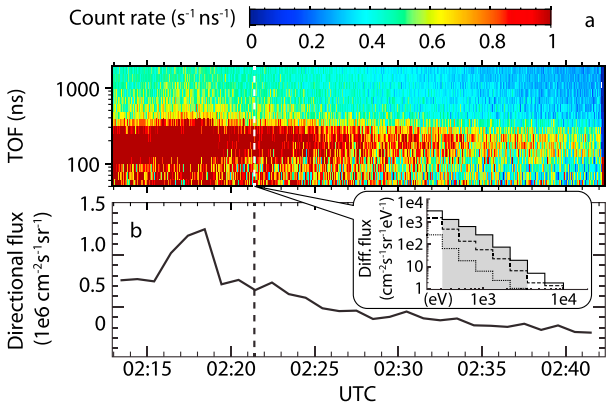

Figure 4. (a) E-t spectrum and (b) directional flux measured in the anomalies case shown in Figure 3. The structure of the figure is the same as Figure 2 except that the extra dashed line in the energy spectrum panel shows the energy spectrum in the nominal case for comparison.

4. Statistical Results: Longitudinal Variation of ENA Source Intensity

4.1. ENA Flux Backtracing

For a statistical analysis of the magnetic anomaly influence on the ENA emissions,

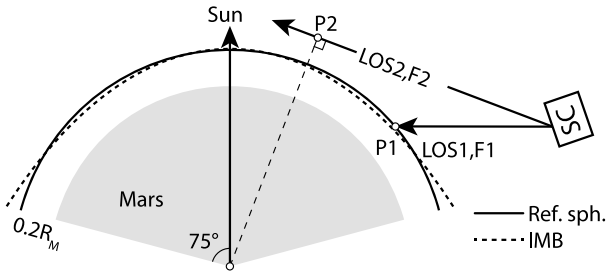

Figure 5. Illustration of source region position (P1 and P2) for the measured ENA flux (F1 and F2) at the spacecraft (SC). The solid curve is the reference sphere at 0.2 R_M altitude that we assumed for representing the IMB. The dashed curve is the average shape of the IMB measured by Mars Express [*Dubinin et al.*, 2006]. The sizes and shapes of Mars (dark shaded fan), the reference sphere, and the IMB are to scale. LOS1 and LOS2 represent two types of lines of sight (LOSs). See the text for details.

we first develop a procedure to map locally measured ENA fluxes in the geographic coordinate system. The observed differential flux intensity in an instrument sector is the integral of local neutral gas density and the proton fluxes over its lines of sight (LOSs); therefore, the position of the source along the LOS is unknown. Fortunately, previous observations and simulations showed that the majority of dayside ENAs are emitted near the dayside IMB (~0.2 R_M altitude) [*Kallio et al.*, 1997; *Gunell et al.*, 2006a; *Futaana et al.*, 2006b] where the neutral density is the highest (lowest altitude) and the proton flux is still significant (protons do not penetrate the IMB). Some simulations showed that the most intense source region locates between the bow shock and the IMB, from the subsolar point to a SZA of ~ 75° [*Kallio et al.*, 1997; *Mura et al.*, 2002; *Holmström and Kallio*, 2004; *Gunell et al.*, 2006b]. With this knowledge, we define the source position of the ENAs as (1) the intersection (P1) of its corresponding LOS (LOS1) and the IMB, if they intersect, or (2) the point of the closest approach (P2) of the LOS (LOS2) to the center of Mars, if the LOS and the IMB do not intersect (Figure 5). The intensity of the source can thus be described by the flux of the measured ENAs (F1 and F2, respectively). In case 1, we assume that the ENAs are emitted from the IMB, as revealed by previous observations and simulations. In case 2, we assume a spherically symmetric exosphere, of which the neutral density along the LOS is the highest at P2; therefore, it is the most probable source position for the observed ENAs. In practice, we divide the FOV of a sector into many LOSs, each of which is 2° apart. For each LOS we apply the backtracing method mentioned above and locate its source position in the geographic coordinate system. We exclude the data from a sector if none of its LOSs intersect with the IMB at all.

Figure 6 shows the results of the source region projection for the nominal and the anomaly case. Consistent with Figures 1 and 3, the source region of ENAs in the nominal case covers the area between 260°E and 310°E, 20°S and 20°N in the geographic coordinate system, while that in the anomaly case covers from 190°E to 250°E in the same latitude band. We use very fine bins to demonstrate the actual shapes of the backtraced source regions in both cases, which are very similar due to very similar observation geometries.

We repeat the backtracing process to all the orbits for the observation period when the solar wind dynamic pressure was lower than 1.8 nPa, to exclude its influence on the ENA flux [*Wang et al.*, 2013]. Most of the selected observations were conducted between 09:00 and 12:00 local time. On each orbit, the source positions cover an area of the similar shape as one in Figure 6. Here we only take the source positions with SZA less than 75°, because (1) we focus on the ENA emission from the dayside hemisphere and (2) other observations may be in a much different observation geometry. In this study we simplify the shape of the IMB to a spherical surface at 0.2 R_M altitude for the simplicity of calculations. This is the average altitude of the IMB over the SZA < 75° above the Mars surface. The deviation of the reference sphere from the actual shape of the IMB is ~0 at the subsolar point and <~ 0.05 R_M (170 km) at 75° SZA. This approximation is valid for the current study because (1) this difference is less than the

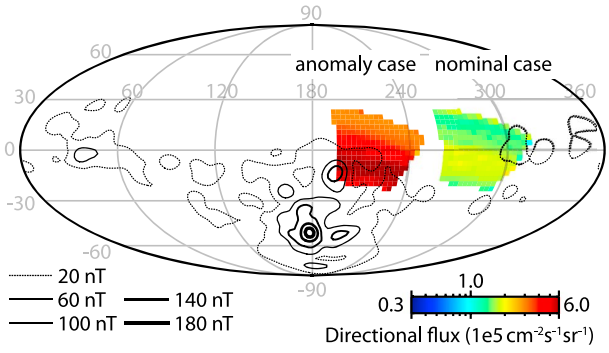

Figure 6. Source positions of ENAs in the nominal case and the anomaly case in the geographic coordinate system. The local times in both cases are the same. Contours show, from the dotted to the thickest curve, the modeled magnetic field intensities of 20, 60, 100, 140, and 180 nT at 400 km altitude derived from the nightside measurement of Mars Global Surveyor [*Lillis et al.*, 2010].

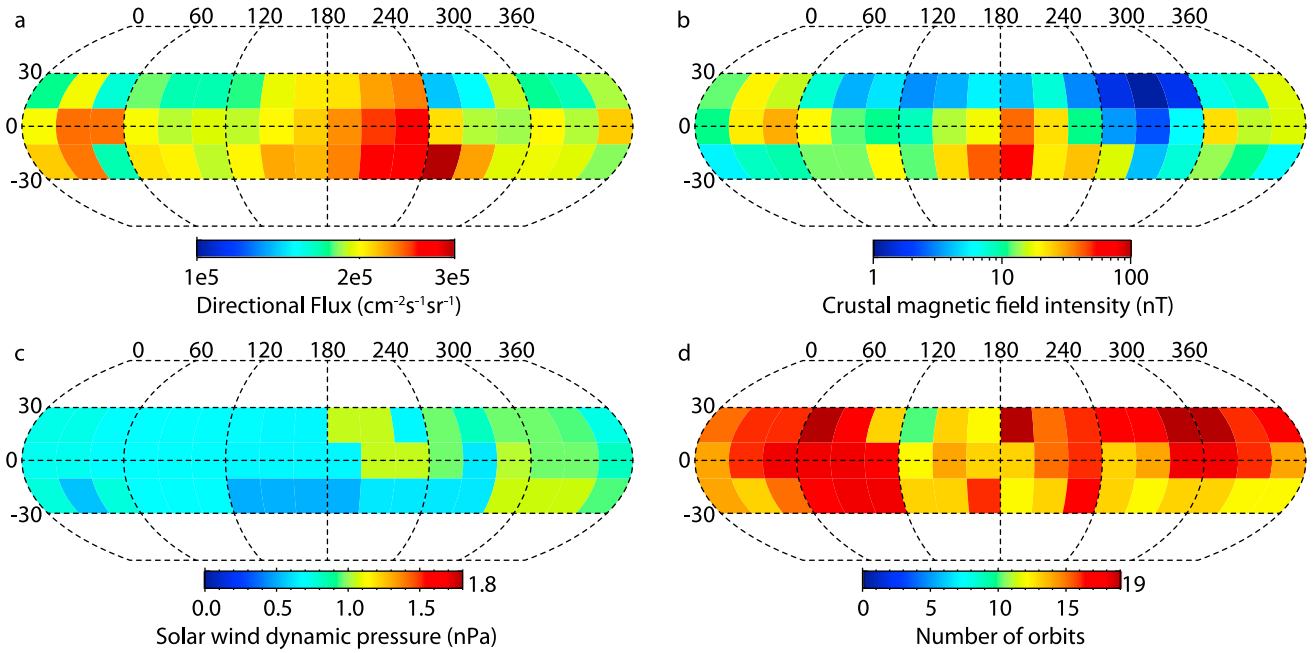

Figure 7. Maps of (a) ENA directional flux, (b) crustal magnetic field intensity, (c) mapped upstream solar wind pressure proxy, and (d) orbit coverage in the geographic coordinates.

scale heights of atomic hydrogen (~ 600 km) and hot atomic oxygen (~ 240 km) [*Feldman et al.*, 2011] which are the major neutrals to produce charge exchange ENAs, (2) the variation of the IMB altitude during the whole observation period is larger than this difference [*Dubinin et al.*, 2006], and (3) the resultant ENA source intensity map is not sensitive to the altitude of IMB. We made a test assuming different reference sphere altitudes (e.g., 0.1 or 0.3 R_M), the results do not change at current resolution (20° × 20°), meaning that the backtracing method is robust under current resolution against different IMB altitudes in a realistic range.

4.2. Statistical Results From the Whole Data Set

So far, we have associated the measured ENA fluxes with the geographic coordinate system by locating their most probably source position. The number of energy spectra, i.e., number of projection positions, ranges from 600 (10 min observation) to 2000 (30 min observation) per orbit. We then resample all the projection positions with a certain bin size to generate a uniform geographic map. The bin size should be large enough to contain enough flux values from multiple orbits, while small enough to show spatial patterns associated with the magnetic anomalies. After several trials we use a bin size of 20° × 20°, to make sure that every bin has been covered by at least 10 orbits (Figure 7d). Bins outside the latitude band 30°S–30°N are discarded because they are covered by too few orbits. Within each bin, the source positions projected from the same initial directional flux are counted as one measurement. We then calculate the median value of all directional fluxes in each bin for its robustness against extreme values. The results are shown in Figure 7a.

The ENA source intensity expressed by the directional flux shows longitudinal variation in all three latitude bands. The peak-to-valley variation ranges from 45% to 91%. The more intense source regions locate differently among different latitudes, but they all show a peak or a plateau over the 140°E–280°E longitude range. Another more confined region with higher source intensity is evident between 20°E and 60°E, in the 0° and 20°S latitude bands. Figure 8 shows the median value, the 25% and 75% quartiles of the source intensity in the 0° band, all of which show similar variations.

These two regions—140°E–280°E for all latitude bands and 20°E–60°E for 10°S–10°N—coincide with the two strongest crustal magnetic anomaly regions in the selected latitude range. In order to quantify this coincidence, we first down sample the crustal magnetic field intensity into the same resolution as in the flux map (Figure 7b). The magnetic field intensity value in each bin is the median of all raw data points in the model covered by the bin. Here we do not directly correlate the flux in the three latitude bands with the magnetic field intensity in the same bins, because the influence of a stronger crustal magnetic field extends further than a weaker field. Hence, we take the maximum |B| values across the 30°S–30°N for each longitude bin

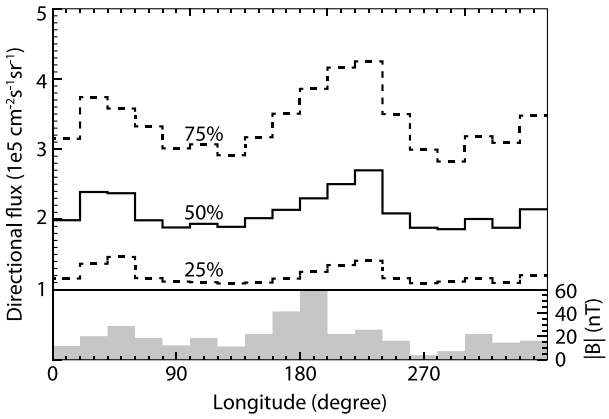

Figure 8. The three quartiles of the source intensity expressed in directional flux as a function of the longitude for the 10°S–10°N bins. The shaded histogram shows the maximum |B| values across the latitudes in Figure 7b.

(shaded histogram in Figure 8) as the reference magnetic field intensity and calculate Spearman's rank correlation coefficients of the ENA fluxes in the three latitude bands with it. The three correlation coefficients for the 20°S, 0°, and 20°N latitudes are, respectively, 0.214, 0.527, and 0.787. The probabilities that the ENA fluxes and the reference magnetic field intensities are correlated by chance under the null hypothesis are $p = 0.395$, < 0.0005, and 0.025, meaning that in the latitude range 10°S–30°N, the correlation is significant according to the $p < 0.05$ criterion. In the 20°S latitude band the correlation is not significant, the reason for which is discussed later.

We also investigate the correlation coefficient between the ENA directional flux and the SWP. We have already excluded all the data obtained when the solar wind dynamic pressure was higher than 1.8 nPa to avoid its influence. However, its residual fluctuation below 1.8 nPa may still contribute to the fluctuation of ENA emission, partly. Here we map the SWP to the geographic coordinates in the similar means to the concurrent ENA measurements (Figure 7c). The correlation coefficients between the ENA directional fluxes in the three latitude bands and corresponding SWP values are −0.099 (20°N, $p = 0.696$), 0.195 (0°, $p = 0.437$), and −0.614 (20° S, $p = 0.007$). The correlations are not significant except for the 20°S latitude band. The insignificance of the correlation indicates that the cleaning of SWP influence is effective. The anticorrelation between the SWP and the ENA flux at 20°S suggests that the observations in this latitude band have been disturbed by the residual fluctuation of the SWP; therefore, the correlation between the ENA flux and the crustal magnetic field intensity becomes less clear.

5. Discussion

The NPD observes enhanced ENA emission associated with the presence of the crustal magnetic anomalies in its FOV. The case studies show that the ENA directional flux in the anomaly case was 4 times higher than that in the nominal case. Statistical study shows the same result that ENA emissions are stronger from the regions with stronger crustal magnetic field.

Longitudinal variations of the neutral atmosphere propagating up to the exosphere may result in the ENA signal increase. The only known phenomenon resulting in the neutral density increase at certain geographic longitudes is nonmigrating tides [cf. *Forbes*, 2004]. However, the longitudes of the maximum neutral density associated with these tides are ∼ 90° and ∼ 270° [*Forbes*, 2004], whereas we observe ENA enhancements in 20°–60° and 140°–280°. Thus, nonmigrating tides cannot be responsible for the observed ENA flux enhancement.

From the mapping of the ENA flux observed by Mars Express/NPD data set, apparent enhancements of the ENA flux, coinciding with the magnetic anomaly locations, are identified. We briefly discuss the two potential mechanisms that may consistently explain the observed apparent enhancement of ENA flux above the magnetic anomalies: (1) the deflection of the highly directional plasma flow above anomalies toward the detectors and (2) increase of exospheric densities above the anomalies.

The plasma flow in the magnetosheath is anisotropic because the proton thermal velocity is much smaller than the bulk velocity except for the region close to the stagnation point of the magnetopause. The resultant charge exchange ENA flux is therefore anisotropic and resembles a beam or jet [*Futaana et al.*, 2006a] along the direction tangential to the solar wind flow direction. If the spacecraft is outside the ENA beam, only a small fraction of the flux resulting from thermal spreading of the original protons population can be observed (Figure 9a). On the other hand, complex structures of the anomalies' magnetic field and its interaction with the magnetosheath plasma result in highly irregular plasma flow pattern above magnetic

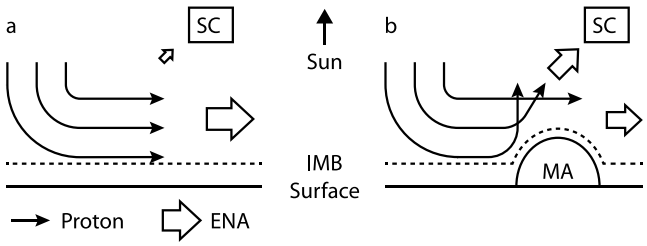

Figure 9. Sketch for the deviation of the proton velocity toward the detector caused by the magnetic anomalies. The solid curves with arrows represent streamlines of protons in the magnetosheath. The open arrow represents ENA fluxes, and its size illustrates the flux value. (a) The spacecraft only detects low ENA flux without magnetic anomalies; (b) the deviation of the proton flow due to presence of the magnetic anomalies provides higher flux to the spacecraft.

anomalies. Such irregular plasma flows can produce ENAs with a wide direction spread, and therefore, a higher flux can be now detected from the same position (Figure 9b). If this mechanism acts on, the ENA source regions influenced by magnetic anomalies may exceed the area of the magnetic anomalies on the surface of Mars; therefore, the enhancement of ENAs in Figure 7a does not strictly cover the magnetic anomalies.

Another possible mechanism is the enhancement of the exosphere density caused by the existing of magnetic anomalies. One possible source of the enhanced neutral density is the heating and sputtering of the atmosphere by the precipitating magnetosheath plasma. The heating would elevate the altitude of the exobase and increase the exospheric scale height and thus locally increase the exospheric density above the IMB [*Ness et al.*, 2000; *Krymskii et al.*, 2004]. However, these enhancements are expected to be negligible since the local cusp regions are much smaller in comparison to the total area of the magnetic anomalies [*Brain et al.*, 2007], and instances of large scale heights are rare according to radio occultation observations [*Ness et al.*, 2000]. Enhancements of the neutral density due to sputtering are also expected to be negligible for nominal solar conditions at Mars [*Johnson et al.*, 2008; *Wang et al.*, 2014]. Another source of the exospheric density enhancement is via the modification of chemical reactions in the magnetic anomaly regions with closed field lines. The magnetic field can confine the ionospheric electrons and prohibit their vertical transport, changing the ionospheric density profile with respect to nonmagnetized regions. The change of the ionospheric profile alters the neutral gas profiles and ENA production rate via charge exchange. If the plasma flow pattern keeps the same in the anomaly case, an increase of 4 times in the detected ENA in the anomaly case means that the ENA production rate can vary in a comparable ratio. If we assume the directionality of ENA emission to be the same as in *Wang et al.* [2013], and the source region is the magnetosheath with a SZA less than 75°, we can derive the dayside ENA emission rate to be 2.1×10^{23} s^{-1} and 8.4×10^{23} s^{-1} for the nominal case and the anomaly case, respectively. The enhancement in the neutral atmosphere should be also comparable. The effects of magnetic anomalies on the neutral atmosphere have not been studied comprehensively. Modern optical spectrometry and ionospheric sounding experiments are suitable to verify this hypothesis.

6. Conclusion

Using measurements of the ENA differential flux data from MEX/ASPERA-3/NPD during stable solar wind conditions and low solar wind dynamic pressure (<1.8 nPa) we identified the ENA enhancement events when the crustal magnetic anomalies face the Sun and close to the FOV of NPD. We further revealed the distribution of the ENA emission intensity expressed by the ENA directional flux backtraced to its source positions close to the IMB, in a planetary coordinate system. In the longitude ranges 20°E–60°E and 140°E–280°E between 30°S and 30°N, the ENA flux shows two maxima, with a peak-to-valley ratio of 1.4–1.9. These two ENA flux enhancements coincide with the two strongest crustal magnetic anomaly regions. In two of three latitude bands, the correlation between the ENA flux and the magnetic field intensity is significant, while in the other latitude band the ENA flux may have been disturbed by the residual fluctuation of the SWP. The physical relations between the ENA emission and the crustal magnetic anomalies, in addition to the verification of the correlation itself, need further studies. Two possible mechanisms explaining the ENA flux enhancement have been proposed, namely, the deviation of the proton velocity caused by irregular magnetosheath plasma flows in the anomaly regions and an increase in the exospheric density close to the magnetic anomalies. In situ plasma measurements in the anomaly regions and remote spectroscopic observations can test these hypotheses.

Acknowledgments
This work is supported by Swedish National Space Board via the contract 107/12 of 2012-12-18. The NPD data can be obtained on request to Mats Holmström (ASPERA-3 PI, matsh@irf.se) of the Swedish Institute of Space Physics. The authors thank D. Crider and D. Brain for providing the solar wind pressure proxy at Mars.

Michael Liemohn thanks the reviewers for their assistance in evaluating this paper.

References

Acuña, M. H., et al. (1998), Magnetic field and plasma observations at Mars: Initial results of the Mars Global Surveyor mission, *Science*, *279*(5357), 1676–1680, doi:10.1126/science.279.5357.1676.

Barabash, S., M. Holmström, A. Lukyanov, and E. Kallio (2002), Energetic neutral atoms at Mars 4. Imaging of planetary oxygen, *J. Geophys. Res.*, *107*(A10), 1280, doi:10.1029/2001JA000326.

Barabash, S., et al. (2006), The Analyzer of Space Plasmas and Energetic Atoms (ASPERA-3) for the Mars Express mission, *Space Sci. Rev.*, *126*(1-4), 113–164.

Brain, D., J. Halekas, R. Lillis, D. Mitchell, R. Lin, and D. Crider (2005), Variability of the altitude of the Martian sheath, *Geophys. Res. Lett.*, *32*, L18203, doi:10.1029/2005GL023126.

Brain, D. A., F. Bagenal, M. H. Acuña, and J. E. P. Connerney (2003), Martian magnetic morphology: Contributions from the solar wind and crust, *J. Geophys. Res.*, *108*(A12), 1424, doi:10.1029/2002JA009482.

Brain, D. A., R. J. Lillis, D. L. Mitchell, J. S. Halekas, and R. P. Lin (2007), Electron pitch angle distributions as indicators of magnetic field topology near Mars, *J. Geophys. Res.*, *112*, A09201, doi:10.1029/2007JA012435.

Crider, D. H., et al. (2002), Observations of the latitude dependence of the location of the Martian magnetic pileup boundary, *Geophys. Res. Lett.*, *29*(8), 1170, doi:10.1029/2001GL013860.

Crider, D. H., D. Vignes, A. M. Krymskii, T. K. Breus, N. F. Ness, D. L. Mitchell, J. A. Slavin, and M. H. Acuna (2003), A proxy for determining solar wind dynamic pressure at Mars using Mars Global Surveyor data, *J. Geophys. Res.*, *108*(A12), 1461, doi:10.1029/2003JA009875.

Dubinin, E., M. Fränz, J. Woch, E. Roussos, S. Barabash, R. Lundin, J. Winningham, R. Frahm, and M. Acuña (2006), Plasma morphology at Mars. ASPERA-3 observations, *Space Sci. Rev.*, *126*, 209–238, doi:10.1007/s11214-006-9039-4.

Feldman, P. D., et al. (2011), Rosetta-Alice observations of exospheric hydrogen and oxygen on Mars, *Icarus*, *214*(2), 394–399, doi:10.1016/j.icarus.2011.06.013.

Forbes, J. M. (2004), Tides in the middle and upper atmospheres of Mars and Venus, *Adv. Space Res.*, *33*(2), 125–131, doi:10.1016/j.asr.2003.05.007.

Futaana, Y., et al. (2006a), First ENA observations at Mars: Subsolar ENA jet, *Icarus*, *182*(2), 413–423, doi:10.1016/j.icarus.2005.08.024.

Futaana, Y., S. Barabash, A. Grigoriev, D. Winningham, R. Frahm, M. Yamauchi, and R. Lundin (2006b), Global response of Martian plasma environment to an interplanetary structure: From ENA and plasma observations at Mars, *Space Sci. Rev.*, *126*, 315–332, doi:10.1007/s11214-006-9026-9.

Futaana, Y., et al. (2006c), First ENA observations at Mars: ENA emissions from the Martian upper atmosphere, *Icarus*, *182*(2), 424–430, doi:10.1016/j.icarus.2005.09.019.

Futaana, Y., et al. (2008), Mars Express and Venus Express multi-point observations of geoeffective solar flare events in December 2006, *Planet. Space Sci.*, *56*(6), 873–880.

Futaana, Y., J.-Y. Chaufray, H. Smith, P. Garnier, H. Lichtenegger, M. Delva, H. Gröller, and A. Mura (2011), Exospheres and energetic neutral atoms of Mars, Venus and Titan, *Space Sci. Rev.*, *162*(1), 213–266, doi:10.1007/s11214-011-9834-4.

Galli, A., P. Wurz, S. Barabash, A. Grigoriev, H. Gunell, R. Lundin, M. Holmström, and A. Fedorov (2006), Energetic hydrogen and oxygen atoms observed on the nightside of Mars, *Space Sci. Rev.*, *126*, 267–297, doi:10.1007/s11214-006-9088-8.

Galli, A., P. Wurz, E. Kallio, A. Ekenbäck, M. Holmström, S. Barabash, A. Grigoriev, Y. Futaana, M.-C. Fok, and H. Gunell (2008), Tailward flow of energetic neutral atoms observed at Mars, *J. Geophys. Res.*, *113*, E12012, doi:10.1029/2008JE003139.

Grigoriev, A. (2007), The neutral particle detector on the Mars and Venus express missions, Swedish Institute of Space Physics, Kiruna, Sweden.

Grigoriev, A., Y. Futaana, S. Barabash, and A. Fedorov (2006), Observations of the Martian subsolar ENA Jet Oscillations, *Space Sci. Rev.*, *126*(1), 299–313, doi:10.1007/s11214-006-9121-y.

Gunell, H., et al. (2006a), First ENA observations at Mars: Charge exchange ENAs produced in the magnetosheath, *Icarus*, *182*(2), 431–438.

Gunell, H., M. Holmström, S. Barabash, E. Kallio, P. Janhunen, A. F. Nagy, and Y. Ma (2006b), Planetary ENA imaging: Effects of different interaction models for Mars, *Planet. Space Sci.*, *54*(2), 117–131.

Holmström, M., and E. Kallio (2004), The solar wind interaction with Venus and Mars: Energetic neutral atom and X-ray imaging, *Adv. Space Res.*, *33*(2), 187–193.

Johnson, R., M. Combi, J. Fox, W.-H. Ip, F. Leblanc, M. McGrath, V. Shematovich, D. Strobel, and J. H. Waite Jr. (2008), Exospheres and atmospheric escape, *Space Sci. Rev.*, *139*(1-4), 355–397.

Kallio, E., J. G. Luhmann, and S. Barabash (1997), Charge exchange near Mars: The solar wind absorption and energetic neutral atom production, *J. Geophys. Res.*, *102*(A10), 22,183–22,197, doi:10.1029/97JA01662.

Krymskii, A. M., T. K. Breus, N. F. Ness, M. H. Acuña, J. E. P. Connerney, D. H. Crider, D. L. Mitchell, and S. J. Bauer (2002), Structure of the magnetic field fluxes connected with crustal magnetization and topside ionosphere at Mars, *J. Geophys. Res.*, *107*(A9), 1245, doi:10.1029/2001JA000239.

Krymskii, A. M., T. K. Breus, N. F. Ness, D. P. Hinson, and D. I. Bojkov (2003), Effect of crustal magnetic fields on the near terminator ionosphere at Mars: Comparison of in situ magnetic field measurements with the data of radio science experiments on board Mars Global Surveyor, *J. Geophys. Res.*, *108*(A12), 1431, doi:10.1029/2002JA009662.

Krymskii, A. M., N. F. Ness, D. H. Crider, T. K. Breus, M. H. Acuña, and D. P. Hinson (2004), Solar wind interaction with the ionosphere/atmosphere and crustal magnetic fields at Mars: Mars Global Surveyor Magnetometer/Electron Reflectometer, radio science, and accelerometer data, *J. Geophys. Res.*, *109*, A11306, doi:10.1029/2004JA010420.

Lillis, R. J., M. E. Purucker, J. S. Halekas, K. L. Louzada, S. T. Stewart Mukhopadhyay, M. Manga, and H. V. Frey (2010), Study of impact demagnetization at Mars using Monte Carlo modeling and multiple altitude data, *J. Geophys. Res.*, *115*, E07007, doi:10.1029/2009JE003556.

Mitchell, D. L., R. P. Lin, C. Mazelle, H. Réme, P. A. Cloutier, J. E. P. Connerney, M. H. Acuna, and N. F. Ness (2001), Probing Mars' crustal magnetic field and ionosphere with the MGS Electron Reflectometer, *J. Geophys. Res.*, *106*(E10), 23,419–23,427, doi:10.1029/2000JE001435.

Mura, A., A. Milillo, S. Orsini, E. Kallio, and S. Barabash (2002), Energetic neutral atoms at Mars 2. Imaging of the solar wind-Phobos interaction, *J. Geophys. Res.*, *107*, 1278, doi:10.1029/2001JA000328.

Mura, A., et al. (2008), ENA detection in the dayside of Mars: ASPERA-3 NPD statistical study, *Planet. Space Sci.*, *56*(6), 840–845.

Ness, N. F., M. H. Acuña, J. E. P. Connerney, A. J. Kliore, T. K. Breus, A. M. Krymskii, P. Cloutier, and S. J. Bauer (2000), Effects of magnetic anomalies discovered at Mars on the structure of the Martian ionosphere and solar wind interaction as follows from radio occultation experiments, *J. Geophys. Res.*, *105*(A7), 15,991–16,004.

Soobiah, Y., et al. (2006), Observations of magnetic anomaly signatures in Mars Express ASPERA-3 ELS data, *Icarus*, *182*(2), 396–405, doi:10.1016/j.icarus.2005.10.034.

Wang, X.-D., S. Barabash, Y. Futaana, A. Grigoriev, and P. Wurz (2013), Directionality and variability of energetic neutral hydrogen fluxes observed by Mars Express, *J. Geophys. Res. Space Physics*, *118*, 7635–7642, doi:10.1002/2013JA018876.

Wang, Y.-C., J. G. Luhmann, F. Leblanc, X. Fang, R. E. Johnson, Y. Ma, W.-H. Ip, and L. Li (2014), Modeling of the o^+ pickup ion sputtering efficiency dependence on solar wind conditions for the Martian atmosphere, *J. Geophys. Res. Planets*, *119*, 93–108, doi:10.1002/2013JE004413.